# A novel quasi-zero-stiffness strut and its applications in six-degree-of-freedom vibration isolation platform

Jiaxi Zhou[*1], Qingyu Xiao[1], Daolin Xu [*1, 2], Huajiang Ouyang [3], Yingli Li [4]

[1] *College of Mechanical and Vehicle Engineering, Hunan University, Changsha 410082, PR China,*

[2] *State Key Laboratory of Advanced Design and Manufacturing for Vehicle Body, Changsha 410082, PR China,*

[3] *School of Engineering, University of Liverpool, Liverpool L69 3GH, UK*

[4] *School of Traffic and Transportation Engineering, Central South University, Changsha 410082, PR China*

**Abstract** Generally, existing isolators with quasi-zero stiffness (QZS) are designed for mitigating transmission of vertical translational excitations, but vibration isolation in multiple directions is much more desirable and useful. The major contribution of this paper is extending the QZS vibration isolation method from one degree of freedom (DOF) to all six DOFs, by using a novel QZS strut to construct a 6-DOF QZS vibration isolation platform. Firstly, the design concept of the QZS strut is proposed, and then a pyramidal 3-QZS-strut isolator is assembled. Finally, a 6-DOF QZS platform is achieved by using such isolators as supporting mounts. The equations of motion of this platform are established, and solved by the Harmonic Balance method to obtain amplitude-frequency relationships. Moreover, the performance of vibration isolation is evaluated in terms of force/moment transmissibility. Compared with the linear counterpart, the 6-DOF QZS platform has broader bandwidth of vibration isolation starting from lower frequency, and possesses higher effectiveness in low-frequency range, most importantly, in all six DOFs.

**Keywords:** multi-direction vibration isolation, negative-stiffness mechanism, quasi-zero-stiffness strut, transmissibility

[*] Corresponding author. College of Mechanical and Vehicle Engineering, Hunan University, Changsha 410082, PR China.

E-mail address: jxizhou@hnu.edu.cn (Jiaxi Zhou); dlxu@hnu.edu.cn (Daolin Xu).

## 1. Introduction

Recently, a category of vibration isolators with quasi-zero stiffness has been proposed to overcome the drawback of traditional linear passive isolators [1, 2]. Specifically, the QZS isolator not only can attenuate transmission of low-frequency excitations, but also possesses high static stiffness to prevent the system from producing large static deflections. The vital component of a QZS isolator is the negative-stiffness mechanism. There exist several formulas to realize a negative-stiffness mechanism [1, 2]. The earliest form might be the oblique-spring mechanism [3], which was often utilized as a theoretical model for performance evaluation of the QZS isolator [4-7]. To avoid possible bulking of oblique springs, its alternatives can be a planar spring [8], or an oblique link connecting horizontal spring [9]. Other means of negative stiffness include: cam-roller-spring mechanism (CRSM) [10, 11], bi-stable structures [12-16], magnetic springs [17-21], and scissor-like structures [22, 23]. All these investigations indicate that the QZS isolator can perform a good function of low-frequency vibration isolation.

Generally, most of the exiting QZS isolators were designed for mitigating the transmission of vertical translational excitations. However, in many engineering fields including high-technology manufacturing [19, 24], high precision measurement [25] and micro-vibration control in spacecraft [26, 27], multi-direction isolation with high effectiveness is desired to reduce vibration transmission in multiple directions. Hoque et al. [28] developed a 6-DOF hybrid vibration isolation system, which was a combination of an active negative suspension and an active-passive positive suspension with a passive weight support mechanism. Wang and Liu [24] proposed a 6-DOF hybrid micro-vibration isolation platform consisting of passive air springs and magnetostrictive actuators. To attenuate micro-vibration in multiple directions resulting from the reaction and moment wheels on board of spacecraft, Zhou and Li [26] designed and analysed an intelligent vibration isolation platform.

It can be observed from the above works that researchers often resort to active control for multi-direction vibration attenuation. To the best of our knowledge, the designs and studies of passive multi-direction QZS isolators are rarely reported. Sun and Jing [29] designed a 3-DOF QZS isolator in the form of a scissor-like structure. Platus [12] proposed a compact 6-DOF QZS isolator with buckled Euler beams. Zhu et al. [30] developed a 6-DOF QZS/ZS isolator using magnetic levitation. Wu et al. [31] used X-shape structures as the legs to assemble a 6-DOF QZS Stewart platform.

The major contribution of this paper is extending the QZS vibration isolation method from one direction to six directions. The design concept of a novel compact QZS strut is proposed based on the CRSM that has been validated by experimental tests in our previous work [10]. A pyramidal isolator consisting of such three QZS struts is assembled to be a mount to symmetrically support a platform, leading to a 6-DOF QZS vibration isolation platform. The static and dynamic characteristics of this platform are studied, and its isolation performance is theoretically and numerically evaluated in terms of force and moment transmissibility.

The aim of this paper is to show a procedure for creating a 6-DOF QZS vibration isolation platform by using the proposed QZS struts, rather than an experimental study based on a fabricated prototype. In the present study, some assumptions should be noted, which are listed as follows: (1) The deformations of struts are far smaller than the length of the strut, and thus can be approximated by the first order Taylor polynomial. (2) All the QZS struts are identical to each other, and all the inclination angles of the struts with respect to the vertical direction are the same at the static equilibrium. (3) An equivalent constant viscous damping model is assumed for the proposed QZS platform. The actual damping needs to be obtained by experimental measurement on an actual prototype to be built later.

## 2. QZS strut

### 2.1 Conceptual model of the QZS strut

A schematic diagram of the QZS strut is shown in Fig.1. Rigid rod (2) with a cam (9) can only slide along the axial direction guided by two linear bearings (6), which are fixed on sleeves (3). Flexible beams (7) with rollers (8) are fixed on holders (10), which are also fastened on sleeve (3) by screws. There are three flexible beams fixed on annular holders (10) at equal intervals. A coil spring (4) is installed at the end of the strut, and is fastened on the end of rod (2). An adjustor (5) is designed to tune up the compression of coil spring (4) to handle different levels of payload. To assemble a vibration isolation platform by using such QZS struts, ball joints (1) are set at two ends of the strut.

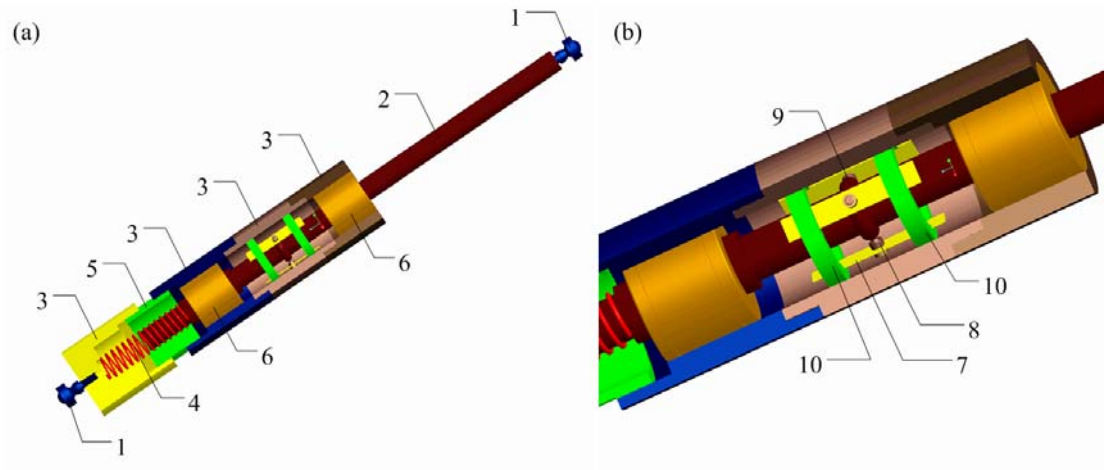


Fig 1 Schematic diagram of QZS strut at the static equilibrium position. (a) Internal configuration; (b) a partially enlarged view. 1 ball joint, 2 rod, 3 sleeve, 4 coil spring, 5 adjuster, 6 linear bearings, 7 flexible beam, 8 roller fixed on the beam, 9 cam fixed on the rod, 10 holder of flexible beams.

### 2.2 Static analysis

The schematic diagram of static analysis is shown in Fig 2. The QZS characteristics are fulfilled by means of a Cam-Roller-Spring Mechanism proposed in our previous

work [10]. When the strut is subjected to a payload $F_P$, the connecting line between the centres of the semi-circular cam and the roller is perpendicular to the axis of the strut, leading to a static equilibrium, as shown in Fig. 2a. At this position, the coil spring with stiffness $k_v$ undergoes a compression of $\Delta_a = F_P / k_v$. When an additional force $f$ is applied on the strut, the rod moves along the axis with a displacement $x$, as illustrated in Fig. 2b. In such situation, the static analyses of the rod and the flexible beam are illustrated in Fig. 2c.

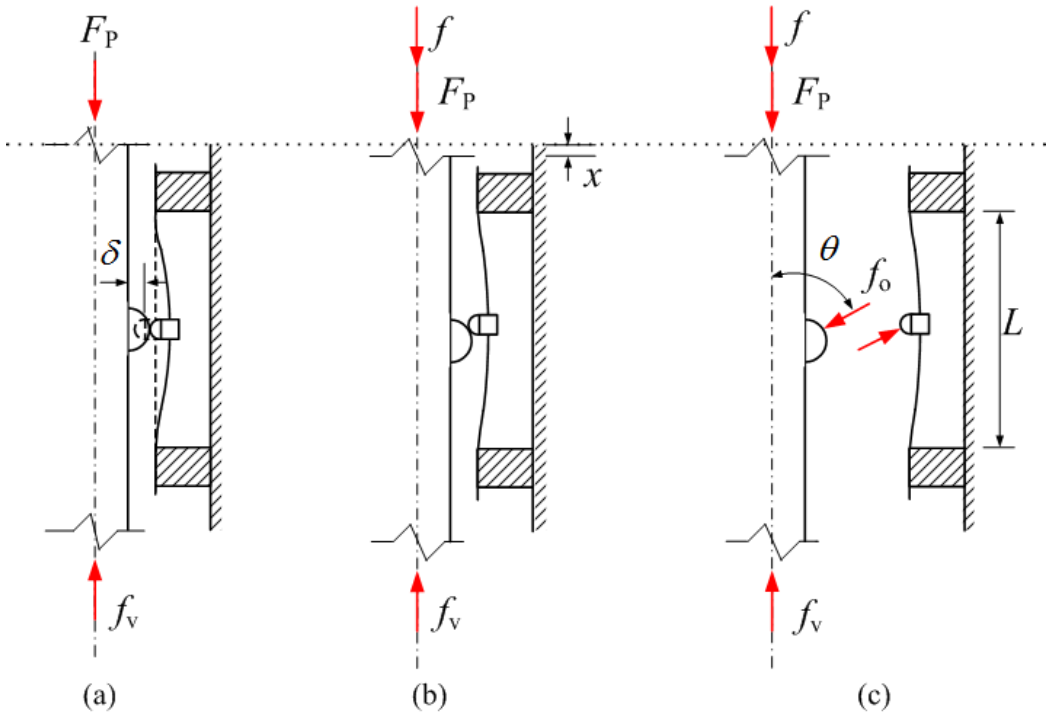


Fig 2 Schematic diagram of static analysis. (a) Static equilibrium position; (b) an external force $f$ applied on the strut results in a compression $x$; (c) forces applied on the rod and the flexible beam.

The static equilibrium equation of the rod is given by

$$f + F_P + 3 f_o \cos\theta - f_v = 0 \tag{1}$$

where $f_o$ is an interaction force between the roller and the cam, $\theta$ is the angle between the axis of the rod and the direction of $f_o$, and $f_v$ is the restoring force of the coil spring. Substituting $f_v = k_v(\Delta_a + x)$ and $F_P = k_v \Delta_a$ into Eq. (1) gives

$$f = k_{\mathrm{v}} x - 3 f_{\mathrm{o}} \cos\theta \tag{2}$$

Then, $f_{\mathrm{o}}$ can be obtained from the static analysis of the clamped flexible beam. By neglecting the distance between the acting point of $f_{\mathrm{o}}$ and the mid-point of the beam, the deflection at the mid-span, namely the displacement of the roller along the direction perpendicular to the beam axis, can be obtained [32]

$$\Delta_{\mathrm{b}} = \frac{f_{\mathrm{o}} L^3}{192EI} \sin\theta \tag{3}$$

where $L$ is the span of the flexible beam, and $EI$ is the flexural rigidity. Deflection $\Delta_{\mathrm{b}}$ also can be obtained through geometrical analysis,

$$\Delta_{\mathrm{b}} = \sqrt{\left(r_1 + r_2\right)^2 - x^2} - \delta \tag{4}$$

where $r_1$ and $r_2$ are the radii of the roller and semi-circular cam, respectively, and $\delta$ is the distance between the centres of the roller and the cam under the non-deformed configuration, as shown in Fig. 2a. By combining Eq. (3) and Eq. (4), and using $\sin\theta = \sqrt{\left(r_1 + r_2\right)^2 - x^2} \Big/ \left(r_1 + r_2\right)$, one can obtain the expression of force $f_{\mathrm{o}}$ as

$$f_{\mathrm{o}} = \frac{192EI}{L^3} \frac{\left(\sqrt{\left(r_1 + r_2\right)^2 - x^2} - \delta\right)\left(r_1 + r_2\right)}{\sqrt{\left(r_1 + r_2\right)^2 - x^2}} \tag{5}$$

By substituting Eq. (5) into Eq. (2), the relationship between the force *f* and the displacement *x* can be given by

$$f = k_{\mathrm{v}} x - \frac{576EI}{L^3}\left(1 - \frac{\delta}{\sqrt{\left(r_1 + r_2\right)^2 - x^2}}\right) x \tag{6}$$

By introducing $\bar{x} = x \big/ \left(r_1 + r_2\right)$ and $\bar{f} = f \big/ \left[k_{\mathrm{v}}\left(r_1 + r_2\right)\right]$, the non-dimensional force-displacement relationship can be expressed as

$$\bar{f} = \bar{x} - \frac{3}{\alpha}\left(1 - \frac{\bar{\delta}}{\sqrt{1 - \bar{x}^2}}\right)\bar{x} \tag{7}$$

where $\bar{\delta} = \delta/(r_1 + r_2)$ and $\alpha = \dfrac{k_v L^3}{192EI}$. Let $\mathrm{d}\bar{f}/\mathrm{d}\bar{x} = 0$ at $\bar{x} = 0$, and then one can get the zero-stiffness condition,

$$\alpha = 3(1 - \bar{\delta}) \tag{8}$$

It implies that the strut can fulfil the QZS characteristics when the stiffness of the coil spring satisfies Eq. (8). Submitting Eq. (8) into Eq. (7) gives the force-displacement relationship of the QZS strut

$$\bar{f}_{\mathrm{QZS}} = \bar{x} - \frac{1}{1 - \bar{\delta}}\left(1 - \frac{\bar{\delta}}{\sqrt{1 - \bar{x}^2}}\right)\bar{x} \tag{9}$$

and the stiffness can be given by

$$\bar{k}_{\mathrm{QZS}} = \frac{\bar{\delta}}{1 - \bar{\delta}}\left[\frac{1}{\sqrt{(1 - \bar{x}^2)^3}} - 1\right] \tag{10}$$

Note that the cam will disengage from the rollers when the displacement of the rod in the axial direction exceeds a critical value $\bar{x}_c = \sqrt{1 - \bar{\delta}^2}$. After the disengagement, the rod is merely supported by the coil spring, and thereby the stiffness of the strut changes into $k_v$. The complete force-displacement relationship can be written as

$$\bar{f}_{\mathrm{QZS}} = \begin{cases} \bar{x} - \dfrac{1}{1 - \bar{\delta}}\left(1 - \dfrac{\bar{\delta}}{\sqrt{1 - \bar{x}^2}}\right)\bar{x}, & \bar{x} < \bar{x}_c \\ \bar{x}, & \bar{x} \geq \bar{x}_c \end{cases} \tag{11}$$

and then the complete expression of stiffness can be obtained by differentiating the above expression with respect to $\bar{x}$

$$\bar{k}_{\mathrm{QZS}} = \begin{cases} \dfrac{\bar{\delta}}{1 - \bar{\delta}}\left[\dfrac{1}{\sqrt{(1 - \bar{x}^2)^3}} - 1\right], & \bar{x} < \bar{x}_c \\ 1, & \bar{x} \geq \bar{x}_c \end{cases} \tag{12}$$

To simplify the following static and dynamic analysis of the platform, the force-displacement relationship is approximated by a cubic function using a truncated Taylor series expansion about the equilibrium, as given by

$$\bar{f}_{\mathrm{QZS}}=\begin{cases}\gamma\bar{x}^3, & \bar{x}<\bar{x}_c\\ \bar{x}, & \bar{x}\geq\bar{x}_c\end{cases} \tag{13}$$

where $\gamma=\bar{\delta}\big/\left[2\left(1-\bar{\delta}\right)\right]$. And then the simplified expression for stiffness can be readily given by differentiating the above expression with respect to $\bar{x}$

$$\bar{k}_{\mathrm{QZS}}=\begin{cases}3\gamma\bar{x}^2, & \bar{x}<\bar{x}_c\\ 1, & \bar{x}\geq\bar{x}_c\end{cases} \tag{14}$$

To avoid contact between the cam and the flexible beams, the distance between the centre of the cam and the flexible beam under the non-deformed configuration should be larger than the radius of the cam, i.e. $\bar{\delta}\geq\bar{r}_2$, where $\bar{r}_2=r_2\big/\left(r_1+r_2\right)$. The upper limit of $\delta$ is $\left(r_1+r_2\right)$, otherwise the cam will always disengages with the roller. Therefore, $\bar{\delta}$ should be selected within the range of $\left[\bar{r}_2,1\right)$.

Fig. 3 shows the stiffness of the QZS strut for different $\bar{\delta}$ when $\bar{r}_2=2/3$. Obviously, in the vicinity of static equilibrium, the non-dimensional stiffness is below 1, which means the stiffness of the strut is smaller than that of the coil spring. The stiffness curve becomes steep as $\bar{\delta}$ increases, leading to a narrow displacement range of smaller stiffness than that of the coil spring. In addition, the circle denotes the critical value of displacement that allows engagement between the cam and the roller, which implies that the displacement range for engagement is also narrowed by increasing $\bar{\delta}$. Therefore, $\bar{\delta}$ is suggested to be selected as $\bar{r}_2$, due to the degradation of QZS characteristics caused by increasing $\bar{\delta}$.

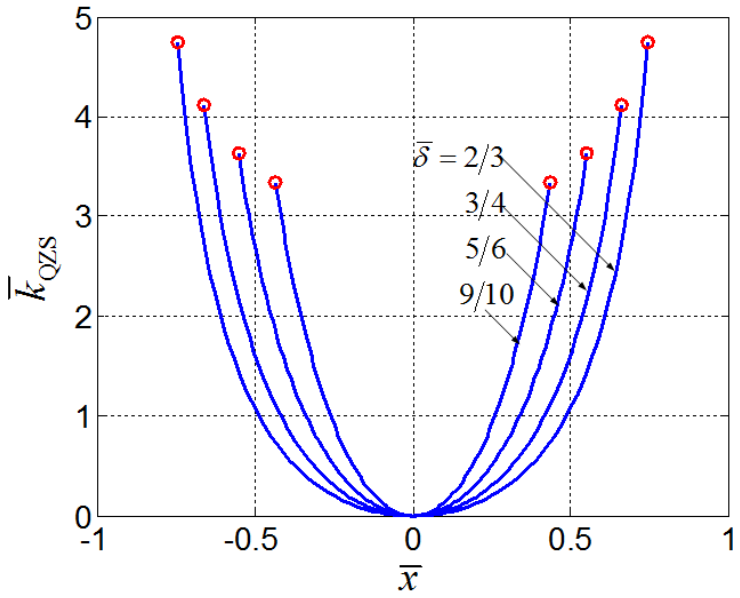


Fig 3 Stiffness of QZS strut for the settings of $\bar{\delta}$ with $\bar{r}_2 = 2/3$.

### 2.3 Stiffness and strength of the flexible beam

The flexible beams are fundamental elements of the CRSM to provide negative stiffness in the axial direction. The zero stiffness condition (Eq. (8)) indicates the requirement on the stiffness of the flexible beam, i. e.

$$\frac{k_v L^3}{48Ebh^3} = \left(1-\bar{\delta}\right) \tag{15}$$

where *b* and *h* are the width and thickness of the beam, respectively. At the static equilibrium position, the maximum stress in the beam arrives at its peak value

$$\sigma_{\max} = 12E\frac{h\left(r_1+r_2\right)}{L^2}\left(1-\bar{\delta}\right) \le \sigma_s \tag{16}$$

where $\sigma_s$ is the allowable stress. Substituting Eq. (15) into Eq. (16) gives

$$\sigma_{\max} = \frac{k_v L\left(r_1+r_2\right)}{4bh^2} \le \sigma_s \tag{17}$$

In the design process, the geometrical parameters, such as width, length and thickness of the beam, should meet with the zero stiffness condition (Eq. (15)) as well as the requirement on the strength (Eq. (17)) simultaneously.

## 3 6-DOF QZS vibration isolation platform

A vibration isolation platform supported by pyramidal 3-QZS-strut isolators is shown in Fig. 4, on which a machine is mounted rigidly. Both the platform and machine are assumed to be rigid bodies with total mass *m*, and located symmetrically. Hence, the whole system is not eccentric. The origin of the coordinate system *x*-*y*-*z* lies at the centroid of the system, and the moments of inertia of the system are designated as $I_x$, $I_y$, and $I_z$. Suppose that the machine generates excitations in 6 DOFs at the centroid of the system, namely $\{F_x(t), F_y(t), F_z(t), M_x(t), M_y(t), M_z(t)\}^{\mathrm{T}}$. The pyramidal 3-QZS-strut isolators are located at four corners of the platform, and its characteristics and configuration are addressed as follows. It is reminded that all the struts are identical to each other, and all the inclination angles with respect to the vertical direction are the same at the static equilibrium.

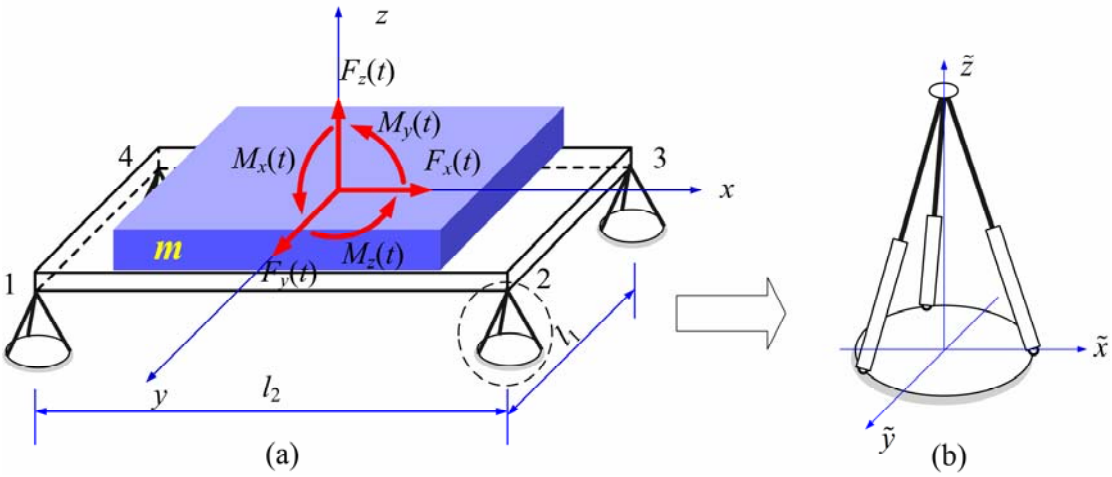


Fig 4 Schematic diagram of (a) the vibration isolation platform supported by (b) pyramidal 3-QZS-struts isolators.

### 3.1 Pyramidal 3-QZS-strut isolator

The proposed pyramidal 3-QZS-struts isolator is shown in Fig. 5a. Both ends of the strut are fixed on two rigid plates by ball joints, respectively. On the surface of the fixed rigid plate (bottom one), the ball joints are evenly distributed. On the movable rigid plate (top one), the ball joints are made to stay closely, and hence all the axes of

the three QZS struts can be supposed to intersect at one point. All the angles between each axis of the QZS strut and the $\tilde{z}$ axis are $\phi$. Considering the situation of small deformation, the disengagement between the roller and the cam would not occur in the following static analysis, and thus the first simplified expression (in Eq. (13)) of the restoring force is adopted.

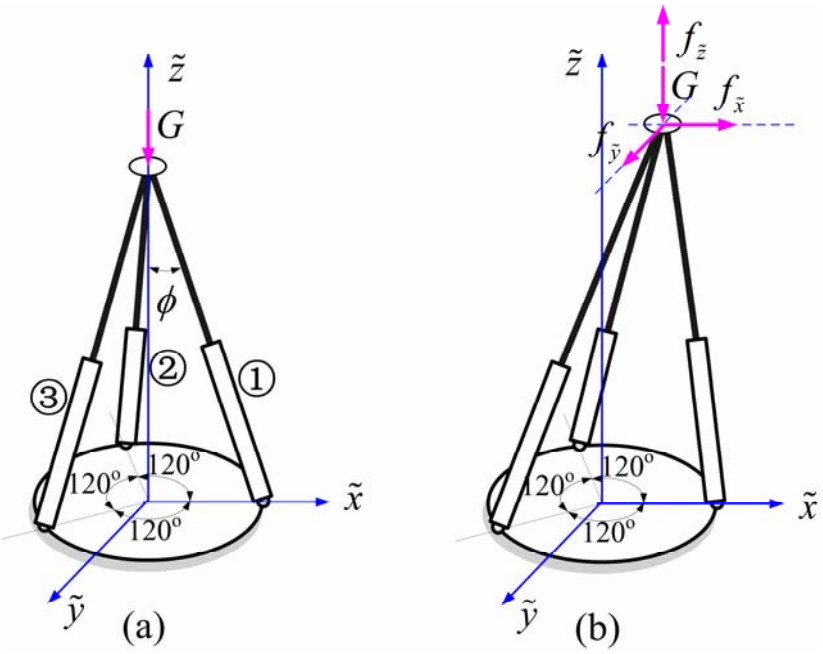


Fig 5 (a) Pyramidal 3-QZS-struts isolator in static equilibrium position under a payload; (b) deformational configuration under the payload and additional loads.

The deformed configuration under the payload and additional loads is shown in Fig. 5b, and the displacement vector of the centre of the top rigid plate is $\{\tilde{x}, \tilde{y}, \tilde{z}\}^{\mathrm{T}}$. Therefore, the axial deformations of the QZS struts can be calculated by

$$\begin{aligned}
\Delta l_1 &= \sqrt{\left(\tilde{x}-R\right)^2+\tilde{y}^{\,2}+\left(\tilde{z}+h\right)^2}-\sqrt{R^2+h^2} \\
\Delta l_2 &= \sqrt{\left(\tilde{x}+R\cos 60^\circ\right)^2+\left(\tilde{y}+R\sin 60^\circ\right)^2+\left(\tilde{z}+h\right)^2}-\sqrt{R^2+h^2} \\
\Delta l_3 &= \sqrt{\left(\tilde{x}+R\cos 60^\circ\right)^2+\left(\tilde{y}-R\sin 60^\circ\right)^2+\left(\tilde{z}+h\right)^2}-\sqrt{R^2+h^2}
\end{aligned} \tag{18}$$

where $R = h\tan\phi$. Because the deformations are far less than the length of the strut, the deformations in Eq. (18) can be approximated by the first order Taylor series at the static equilibrium $(0, 0, 0)$,

$$\begin{aligned}\Delta l_1 &\approx -\tilde{x}\sin\phi+\tilde{z}\cos\phi\\ \Delta l_2 &\approx \frac{1}{2}\tilde{x}\sin\phi+\frac{\sqrt{3}}{2}\tilde{y}\sin\phi+\tilde{z}\cos\phi\\ \Delta l_2 &\approx \frac{1}{2}\tilde{x}\sin\phi-\frac{\sqrt{3}}{2}\tilde{y}\sin\phi+\tilde{z}\cos\phi\end{aligned} \tag{19}$$

The resultant forces in the struts can be given by

$$F_{\mathrm{N}i}=\frac{G}{3\cos\phi}-\Upsilon\Delta l_i^3,\quad i=1,2,3 \tag{20}$$

where $\Upsilon=\gamma k_{\mathrm{v}}/\left(r_1+r_2\right)^2$. The static equilibrium equations of the top rigid plate can be given by

$$\begin{aligned}&-F_{\mathrm{N1}}\sin\phi+\left(F_{\mathrm{N2}}+F_{\mathrm{N3}}\right)\frac{1}{2}\sin\phi+f_{\tilde{x}}=0\\ &\left(F_{\mathrm{N2}}-F_{\mathrm{N3}}\right)\frac{\sqrt{3}}{2}\sin\phi+f_{\tilde{y}}=0\\ &\left(F_{\mathrm{N1}}+F_{\mathrm{N2}}+F_{\mathrm{N3}}\right)\cos\phi+f_{\tilde{z}}-G=0\end{aligned} \tag{21}$$

By substituting Eq.(19) and Eq. (20) into Eq. (21), the expressions of additional loads $\left\{f_{\tilde{x}},\,f_{\tilde{y}},\,f_{\tilde{z}}\right\}^{\mathrm{T}}$ with respect to the displacements $\left\{\tilde{x},\,\tilde{y},\,\tilde{z}\right\}^{\mathrm{T}}$ can be given by

$$\begin{aligned}f_{\tilde{x}}\left(\tilde{x},\,\tilde{y},\,\tilde{z}\right)&=\frac{9}{8}\Upsilon\left(s^4\tilde{x}^3-2s^3c\tilde{x}^2\tilde{z}+s^4\tilde{x}\tilde{y}^2+4s^2c^2\tilde{x}\tilde{z}^2+2s^3c\tilde{y}^2\tilde{z}\right)\\ f_{\tilde{y}}\left(\tilde{x},\,\tilde{y},\,\tilde{z}\right)&=\frac{9}{8}\Upsilon\left(s^4\tilde{y}^3+s^4\tilde{y}\tilde{x}^2+4s^2c^2\tilde{y}\tilde{z}^2+4s^3c\tilde{y}\tilde{x}\tilde{z}\right)\\ f_{\tilde{z}}\left(\tilde{x},\,\tilde{y},\,\tilde{z}\right)&=\frac{3}{4}\Upsilon\left(4c^4\tilde{z}^3+6s^2c^2\tilde{z}\tilde{x}^2+6s^2c^2\tilde{z}\tilde{y}^2-s^3c\tilde{x}^3+3s^3c\tilde{x}\tilde{y}^2\right)\end{aligned} \tag{22}$$

where $s=\sin\phi$ and $c=\cos\phi$. When $\tilde{x}\neq 0,\,\tilde{y}=0,\,\tilde{z}=0$, the applied load along $\tilde{x}$ direction is $f_{\tilde{x}}=\frac{9}{8}\Upsilon s^4\tilde{x}^3$. Similarly, $f_{\tilde{y}}=\frac{9}{8}\Upsilon s^4\tilde{y}^3$ when $\tilde{x}=0,\,\tilde{y}\neq 0,\,\tilde{z}=0$ and $f_{\tilde{z}}=3\Upsilon c^4\tilde{z}^3$ when $\tilde{x}=0,\,\tilde{y}=0,\,\tilde{z}\neq 0$. Therefore, the pyramidal 3-QZS-strut isolator has QZS characteristics in all three translational DOFs.

### 3.2 Static characteristics of the platform

When the loads $\left\{F_x,F_y,F_z,M_x,M_y,M_z\right\}^{\mathrm{T}}$ are applied on the centroid of the

platform, the centroid experiences displacements $\left\{x, y, z, \theta_x, \theta_y, \theta_z\right\}^{\mathrm{T}}$. Since the displacements are far less than the dimensions of the platform, the displacements of the platform at the four support points, which are equal to those of the vertices of the pyramidal 3-QZS-strut isolators accordingly, can be given by

$$\begin{aligned}
&\tilde{x}_1 = x_1 = x + \frac{l_1}{2}\theta_z,\ \tilde{y}_1 = y_1 = y + \frac{l_2}{2}\theta_z,\ \tilde{z}_1 = z_1 = z - \frac{l_1}{2}\theta_x - \frac{l_2}{2}\theta_y \\
&\tilde{x}_2 = x_2 = x + \frac{l_1}{2}\theta_z,\ \tilde{y}_2 = y_2 = y - \frac{l_2}{2}\theta_z,\ \tilde{z}_2 = z_2 = z - \frac{l_1}{2}\theta_x + \frac{l_2}{2}\theta_y \\
&\tilde{x}_3 = x_3 = x - \frac{l_1}{2}\theta_z,\ \tilde{y}_3 = y_3 = y - \frac{l_2}{2}\theta_z,\ \tilde{z}_3 = z_3 = z + \frac{l_1}{2}\theta_x + \frac{l_2}{2}\theta_y \\
&\tilde{x}_4 = x_4 = x - \frac{l_1}{2}\theta_z,\ \tilde{y}_4 = y_4 = y + \frac{l_2}{2}\theta_z,\ \tilde{z}_4 = z_4 = z + \frac{l_1}{2}\theta_x - \frac{l_2}{2}\theta_y
\end{aligned} \tag{23}$$

where subscripts 1, 2, 3, 4 denote the positions of corners, respectively, as shown in Fig. 4a. It is assumed that the distance between the centroids of the machine and the platform $l_{zc}$ is far less than $l_1$ and $l_2$; hence, contributions of $\theta_y$ and $\theta_x$ to $x_i$ and $y_i$ $\left(i = 1 \sim 4\right)$, respectively, can be neglected. By substituting Eq. (23) into Eq. (22), one can obtain the restoring forces of isolators, $f_{\tilde{x}i}\left(\tilde{x}_i, \tilde{y}_i, \tilde{z}_i\right)$, $f_{\tilde{y}i}\left(\tilde{x}_i, \tilde{y}_i, \tilde{z}_i\right)$, and $f_{\tilde{z}i}\left(\tilde{x}_i, \tilde{y}_i, \tilde{z}_i\right)$ ($i = 1 \sim 4$). Then, by using the static equilibrium equations of the platform, the relationships between applied loads and displacements can be given by

$$\begin{aligned}
F_x = \frac{9}{8}\Upsilon\Big[&4s^4x^3 - 8cs^3x^2z + 4s^4xy^2 + 16c^2s^2xz^2 + 8cs^3y^2z + 4l_1^2c^2s^2x\theta_x^2 \\
&+ 4l_2^2c^2s^2x\theta_y^2 + \left(3l_1^2 + l_2^2\right)s^4x\theta_z^2 + 4l_1^2cs^3x\theta_x\theta_z - 8l_1^2c^2s^2z\theta_x\theta_z \\
&- 4l_2^2cs^3y\theta_y\theta_z + 2\left(l_2^2 - l_1^2\right)cs^3z\theta_z^2\Big]
\end{aligned} \tag{24}$$

$$\begin{aligned}
F_y = \frac{9}{8}\Upsilon\Big[&4s^4y^3 + 4s^4yx^2 + 16c^2s^2yz^2 + 16cs^3xyz + 4l_1^2c^2s^2y\theta_x^2 + 4l_2^2c^2s^2y\theta_y^2 \\
&+ \left(l_1^2 + 3l_2^2\right)s^4y\theta_z^2 - 4l_1^2cs^3y\theta_x\theta_z - 4l_2^2cs^3x\theta_y\theta_z - 8l_2^2c^2s^2z\theta_y\theta_z\Big]
\end{aligned} \tag{25}$$

$$\begin{aligned}
F_z = \frac{3}{4}\Upsilon\Big[&16c^4z^3 + 24c^2s^2z\left(x^2 + y^2\right) + 12cs^3xy^2 - 4cs^3x^3 + 3\left(l_2^2 - l_1^2\right)cs^3x\theta_z^2 \\
&+ 12l_1^2c^4z\theta_x^2 + 12l_2^2c^4z\theta_y^2 + 6\left(l_1^2 + l_2^2\right)c^2s^2z\theta_z^2 - 12l_1^2c^2s^2x\theta_x\theta_z \\
&- 12l_2^2c^2s^2y\theta_y\theta_z\Big]
\end{aligned} \tag{26}$$

$$M_x=\frac{3}{16}\Upsilon\Big[4l_1^4c^4\theta_x^3+6l_1^4c^2s^2\theta_x\theta_z^2+l_1^2\left(l_1^2-3l_2^2\right)cs^3\theta_z^3+12l_1^2l_2^2c^4\theta_x\theta_y^2 +6l_1^2l_2^2c^2s^2\theta_x\theta_z^2+48l_1^2c^4z^2\theta_x+24l_1^2c^2s^2\left(x^2+y^2\right)\theta_x -48l_1^2c^2s^2xz\theta_z+12l_1^2cs^3\left(x^2-y^2\right)\theta_z\Big] \tag{27}$$

$$M_y=\frac{3}{8}\Upsilon\Big[2l_2^4c^4\theta_y^3+6l_1^2l_2^2c^4\theta_y\theta_x^2+3l_2^2\left(l_1^2+l_2^2\right)c^2s^2\theta_y\theta_z^2+24l_2^2c^4z^2\theta_y +12l_2^2c^2s^2\left(x^2+y^2\right)\theta_y-24l_2^2c^2s^2yz\theta_z-12l_2^2cs^3xy\theta_z\Big] \tag{28}$$

$$M_z=\frac{9}{32}\Upsilon\Big[\left(l_1^2+l_2^2\right)^2s^4\theta_z^3+2l_1^2\left(l_1^2-3l_2^2\right)cs^3\theta_z^2\theta_x+4l_1^2\left(l_1^2+l_2^2\right)c^2s^2\theta_z\theta_x^2 +4l_2^2\left(l_1^2+l_2^2\right)c^2s^2\theta_z\theta_y^2+4\left(3l_1^2+l_2^2\right)s^4\theta_z x^2+4\left(l_1^2+3l_2^2\right)s^4\theta_z y^2 +16\left(l_1^2+l_2^2\right)c^2s^2\theta_z z^2+16\left(l_2^2-l_1^2\right)cs^3\theta_z xz+8l_1^2cs^3\left(x^2-y^2\right)\theta_x -32l_1^2c^2s^2\theta_x xz-32l_2^2c^2s^2\theta_y yz-16l_2^2cs^3\theta_y xy\Big] \tag{29}$$

When the non-zero displacement occurs only in one direction, the above relationships can be simplified as

$$F_x=\frac{9}{2}\Upsilon s^4x^3,\quad \text{when } x\neq 0,\ y=0,\ z=0,\ \theta_x=0,\ \theta_y=0,\ \theta_z=0 \tag{30}$$

$$F_y=\frac{9}{2}\Upsilon s^4y^3,\quad \text{when } x=0,\ y\neq 0,\ z=0,\ \theta_x=0,\ \theta_y=0,\ \theta_z=0 \tag{31}$$

$$F_z=12\Upsilon c^4z^3,\quad \text{when } x=0,\ y=0,\ z\neq 0,\ \theta_x=0,\ \theta_y=0,\ \theta_z=0 \tag{32}$$

$$M_x=\frac{3}{4}\Upsilon l_1^4c^4\theta_x^3,\quad \text{when } x=0,\ y=0,\ z=0,\ \theta_x\neq 0,\ \theta_y=0,\ \theta_z=0 \tag{33}$$

$$M_y=\frac{3}{4}\Upsilon l_2^4c^4\theta_y^3,\quad \text{when } x=0,\ y=0,\ z=0,\ \theta_x=0,\ \theta_y\neq 0,\ \theta_z=0 \tag{34}$$

$$M_z=\frac{9}{32}\Upsilon\left(l_1^2+l_2^2\right)^2s^4\theta_z^3,\quad \text{when } x=0,\ y=0,\ z=0,\ \theta_x=0,\ \theta_y=0,\ \theta_z\neq 0 \tag{35}$$

The stiffness of the platform in each direction can be obtained by differentiating the loads in Eqs.(30)-(35) with respect to the displacement. One can easily find that the stiffness becomes zero at the state equilibrium. Thus, this vibration isolation platform obviously possesses the QZS characteristics in all six DOFs.

### 3.3 Equations of motion of the platform

The displacements of the centroid of the platform are represented as $\mathbf{u}=\left\{x,\ y,\ z,\theta_x,\theta_y,\theta_z\right\}^{\mathrm{T}}$. The equations of motion of the platform can be given by

$$\mathbf{M}\ddot{\mathbf{u}}+\mathbf{K}\mathbf{u}=\mathbf{F} \tag{36}$$

where

$$\begin{aligned}&\mathbf{M}=\mathrm{diag}\left[m,m,m,I_x,I_y,I_z\right],\mathbf{K}=\mathbf{0},\mathbf{F}=\mathbf{F}_t-\mathbf{F}_{\mathrm{R}}\\&\mathbf{F}_t=\left\{F_x(t),F_y(t),F_z(t),M_x(t),M_y(t),M_z(t)\right\}^{\mathrm{T}}\\&\mathbf{F}_{\mathrm{R}}=\left\{F_x(\mathbf{u}),F_y(\mathbf{u}),F_z(\mathbf{u}),M_x(\mathbf{u}),M_y(\mathbf{u}),M_z(\mathbf{u})\right\}^{\mathrm{T}}\end{aligned} \tag{37}$$

where $\mathbf{F}_{\mathrm{R}}$ is the restoring force of the QZS platform, namely Eqs. (24)-(29). It is assumed that all the excitations are harmonic with an identical frequency, namely $\mathbf{F}_t=\mathbf{F}_0\cos(\omega t)$, where $\mathbf{F}_0=\left\{F_{x0},F_{y0},F_{z0},M_{x0},M_{y0},M_{z0}\right\}^{\mathrm{T}}$ are amplitudes of the excitations.

A linear platform is introduced as a counterpart of the QZS platform, which is constructed by removing all negative-stiffness mechanisms, and then the platform is supported just by coil springs with stiffness of $k_{\mathrm{v}}$. The equations of motion of the linear platform can be written as

$$\mathbf{M}\ddot{\mathbf{u}}+\mathbf{K}_{\mathrm{L}}\mathbf{u}=\mathbf{F}_t \tag{38}$$

where

$$\mathbf{K}_{\mathrm{L}}=\mathrm{diag}\left[6s^2k_{\mathrm{v}},6s^2k_{\mathrm{v}},12c^2k_{\mathrm{v}},3c^2l_1^2k_{\mathrm{v}},3c^2l_2^2k_{\mathrm{v}},\frac{3}{2}s^2\left(l_1^2+l_2^2\right)k_{\mathrm{v}}\right] \tag{39}$$

By introducing following non-dimensional terms

$$\begin{aligned}&\overline{x}=\frac{x}{r_1+r_2},\omega_{\mathrm{nz}}=\sqrt{\frac{12k_{\mathrm{v}}\cos^2\phi}{m}},\overline{t}=\omega_{\mathrm{nz}}t,\Omega=\frac{\omega}{\omega_{\mathrm{nz}}},\quad\overline{F}=\frac{F}{12\cos^2\phi k_{\mathrm{v}}\left(r_1+r_2\right)}\\&\overline{M}_j=\frac{M_j}{12\cos^2\phi k_{\mathrm{v}}\left(r_1+r_2\right)^2\overline{I}_j},\overline{I}_j=\frac{I_j}{m\left(r_1+r_2\right)^2},\quad j=x,y,z\end{aligned} \tag{40}$$

where $\omega_{\mathrm{nz}}$ denotes the natural frequency in the *z* DOF of the linear platform, and with the inclusion of an assumed equivalent constant linear viscous damping term $\zeta$ to account for energy dissipation, the equations of motion of the 6-DOF QZS platform can be rewritten as

$$\overline{\mathbf{u}}''+2\zeta\overline{\mathbf{u}}'+\overline{\mathbf{K}}\overline{\mathbf{u}}=\overline{\mathbf{F}} \tag{41}$$

where

$$\begin{aligned}&\bar{\mathbf{u}}=\left\{\bar{x},\bar{y},\bar{z},\theta_x,\theta_y,\theta_z\right\}^{\mathrm{T}},\quad (\bullet)'=\frac{\mathrm{d}}{\mathrm{d}\bar{t}}(\bullet),\quad \boldsymbol{\zeta}=\mathrm{diag}\left[\zeta_1,\zeta_2,\zeta_3,\zeta_4,\zeta_5,\zeta_6\right]\\&\bar{\mathbf{K}}=\mathbf{0},\quad \bar{\mathbf{F}}=\bar{\mathbf{F}}_t-\bar{\mathbf{F}}_{\mathrm{R}}\end{aligned}\tag{42}$$

### 3.3 Fundamental responses

The first approximation of the primary resonance can be derived by using the Harmonic Balance method. Considering the phases between forces and displacements, the fundamental responses are assumed to be

$$\begin{aligned}&\bar{\mathbf{u}}=\bar{\mathbf{U}}_1\cos\Omega\bar{t}+\bar{\mathbf{U}}_2\sin\Omega\bar{t}\\&\bar{\mathbf{U}}_1=\left\{X_1,Y_1,Z_1,\Theta_{x1},\Theta_{y1},\Theta_{z1}\right\}^{\mathrm{T}},\ \bar{\mathbf{U}}_2=\left\{X_2,Y_2,Z_2,\Theta_{x2},\Theta_{y2},\Theta_{z2}\right\}^{\mathrm{T}}\end{aligned}\tag{43}$$

and the amplitudes of the displacements can be written as

$$\bar{\mathbf{U}}=\left\{X,Y,Z,\Theta_x,\Theta_y,\Theta_z\right\}^{\mathrm{T}},\ \bar{\mathbf{U}}(i)=\sqrt{\bar{\mathbf{U}}_1^2(i)+\bar{\mathbf{U}}_2^2(i)},\quad i=1\sim 6\tag{44}$$

Substituting Eq.(43) into Eq. (41) results in

$$\begin{aligned}&-\Omega^2\left(\bar{\mathbf{U}}_1\cos\Omega\bar{t}+\bar{\mathbf{U}}_2\sin\Omega\bar{t}\right)-2\Omega\boldsymbol{\zeta}\left(\bar{\mathbf{U}}_1\sin\Omega\bar{t}-\bar{\mathbf{U}}_2\cos\Omega\bar{t}\right)+\bar{\mathbf{F}}_{\mathrm{R}}\left(\bar{\mathbf{u}}\right)\\&=\bar{\mathbf{F}}_0\cos\Omega\bar{t}\end{aligned}\tag{45}$$

By using $\sin^3\Omega\bar{t}=\left(3\sin\Omega\bar{t}-\sin 3\Omega\bar{t}\right)/4$ , $\cos^3\Omega\bar{t}=\left(3\cos\Omega\bar{t}+\cos 3\Omega\bar{t}\right)/4$ and ignoring the high order harmonic terms, $\bar{\mathbf{F}}_{\mathrm{R}}\left(\bar{\mathbf{u}}\right)$ can be approximated as

$$\bar{\mathbf{F}}_{\mathrm{R}}\left(\bar{\mathbf{u}}\right)\approx\bar{\boldsymbol{\Gamma}}_{\mathrm{R1}}\cos\Omega\bar{t}+\bar{\boldsymbol{\Gamma}}_{\mathrm{R2}}\sin\Omega\bar{t}\tag{46}$$

where $\bar{\boldsymbol{\Gamma}}_{\mathrm{R1}}$ and $\bar{\boldsymbol{\Gamma}}_{\mathrm{R2}}$ are functions of $\bar{\mathbf{U}}_1$ and $\bar{\mathbf{U}}_2$, and independent of time $\bar{t}$. By equating coefficients of $\cos\Omega\bar{t}$ and $\sin\Omega\bar{t}$ in Eq. (44), the amplitude-frequency equations can be given by

$$\begin{cases}-\Omega^2\bar{\mathbf{U}}_1+2\Omega\boldsymbol{\zeta}\bar{\mathbf{U}}_2+\bar{\boldsymbol{\Gamma}}_{\mathrm{R1}}=\bar{\mathbf{F}}_0\\-\Omega^2\bar{\mathbf{U}}_2-2\Omega\boldsymbol{\zeta}\bar{\mathbf{U}}_1+\bar{\boldsymbol{\Gamma}}_{\mathrm{R2}}=\mathbf{0}\end{cases}\tag{47}$$

The above equations are third-order nonlinear algebraic equations of displacement amplitudes $\bar{\mathbf{U}}_1$ and $\bar{\mathbf{U}}_2$, which can be solved numerically. And then, the forces transmitted to the base are given by

$$
\begin{aligned}
\bar{\mathbf{F}}_{\mathrm{T}} &= 2\zeta\bar{\mathbf{u}}' + \bar{\mathbf{F}}_{\mathrm{R}}\left(\bar{\mathbf{u}}\right) \\
&\approx -2\Omega\zeta\left(\bar{\mathbf{U}}_1 \sin\Omega\bar{t} - \bar{\mathbf{U}}_2 \cos\Omega\bar{t}\right) + \left(\bar{\mathbf{\Gamma}}_{\mathrm{R1}} \cos\Omega\bar{t} + \bar{\mathbf{\Gamma}}_{\mathrm{R2}} \sin\Omega\bar{t}\right) \\
&= \left(\bar{\mathbf{\Gamma}}_{\mathrm{R1}} + 2\Omega\zeta\bar{\mathbf{U}}_2\right)\cos\Omega\bar{t} + \left(\bar{\mathbf{\Gamma}}_{\mathrm{R2}} - 2\Omega\zeta\bar{\mathbf{U}}_1\right)\sin\Omega\bar{t} \\
&= \left(\bar{\mathbf{F}}_0 + \Omega^2\bar{\mathbf{U}}_1\right)\cos\Omega\bar{t} + \Omega^2\bar{\mathbf{U}}_2 \sin\Omega\bar{t}
\end{aligned}
\tag{48}
$$

The *i*th component of force/moment transmissibility $\mathbf{T}=\left\{T_{Fx}, T_{Fy}, T_{Fz}, T_{Mx}, T_{My}, T_{Mz}\right\}^{\mathrm{T}}$ can be defined as the ratio of the amplitude of the transmitted force to the excitation amplitude in the form of decibel:

$$
\mathbf{T}(i) = 20\log_{10}\frac{\sqrt{\left[\bar{\mathbf{F}}_0(i) + \Omega^2\bar{\mathbf{U}}_1(i)\right]^2 + \left[\Omega^2\bar{\mathbf{U}}_2(i)\right]^2}}{\bar{\mathbf{F}}_0(i)}, \quad (i = 1 \sim 6) \tag{49}
$$

which is utilized to evaluate the vibration isolation performance in each DOF.

## 4 Numerical Simulations and Discussions

For numerical experiments, a set of parameters of the 6-DOF QZS vibration isolation platform is given in Table 1. The amplitudes of excitation forces are selected as 10% of the total weight of the machine and the platform, and these three forces act at an off-centre location of the platform, which yield three excitation moments. The non-dimensional natural frequencies of the linear platform can be given by $\Omega_{\mathrm{n}x} = \Omega_{\mathrm{n}y} = 0.4082$, $\Omega_{\mathrm{n}z} = 1$, $\Omega_{\mathrm{n}\theta x} = 1.732$, $\Omega_{\mathrm{n}\theta y} = 2.058$, $\Omega_{\mathrm{n}\theta z} = 0.8076$.

Table 1 Parameters of the 6-DOF QZS vibration isolation platform

| Parameter | Value |
|---|---|
| $\bar{\delta}, \gamma, \phi$ | 2/3, 1, $\pi/6$ |
| $\bar{l}_1$, $\bar{l}_2$ | 1000, 2000 |
| $\bar{F}_{x0}$, $\bar{F}_{y0}$, $\bar{F}_{z0}$ | 0.0317, 0.0317, 0.0317 |
| $\bar{M}_{x0}$, $\bar{M}_{y0}$, $\bar{M}_{z0}$ | $1.8998\times10^{-4}$, $6.7051\times10^{-5}$, $4.9559\times10^{-5}$ |
| $\zeta_i, i = 1 \sim 6$ | 0.05 |

It should be noted that angle $\phi$ is an important design parameter for the platform. The stiffness of the linear platform against angle $\phi$ is depicted in Fig. 6. It is

reminded that the QZS platform has the same supporting capability as its linear counterpart. It can be seen that the translational stiffness in the vertical direction $k_z$, and out-of-plane rotational stiffness $k_{\theta x}$ and $k_{\theta y}$ decrease as angle $\phi$ increases. In contrast, the translational stiffness in horizontal directions $k_x$ and $k_y$, and in-plane rotational stiffness $k_{\theta z}$ increase as angle $\phi$ increases.

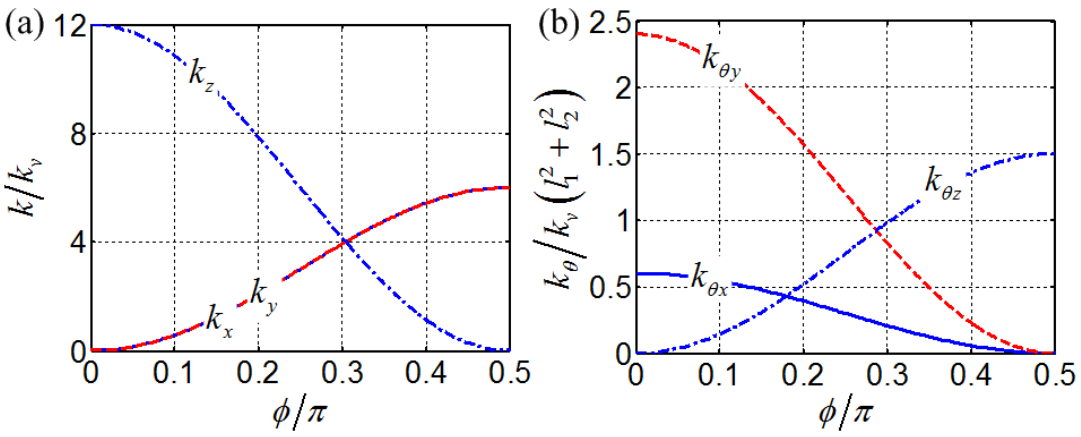


Fig 6 Stiffness of the linear platform against angle $\phi$.

To choose the setting of angle $\phi$, the following considerations should be included when designing this platform. 1) The platform should possess enough stiffness to support the weight of equipment in the vertical direction, and thus one can choose an angle value from the curve $k_z$ subject to the requirement. 2) Another issue is the requirement on the attenuation of vibrations in different directions, which also depends on the situation of actual excitations. For example, if excitations mainly arise from vertical forces ($F_z$) and out-of-plane moments ($M_x, M_y$), thus angle $\phi$ should be selected as a relatively *large* value according to Fig. 6 to achieve better isolation performance; while excitations mainly arise from horizontal forces ($F_x, F_y$) and in-plane moments ($M_z$), angle $\phi$ should be set *small*. (3) One has to consider the balance in designing the angle $\phi$ when there are conflicts among the requirements on the capability of weight support and the types of excitations to be isolated. In this

paper, we do not intend to design a platform for a specific application. Thus the angle is selected as $\pi/6$ here in the purpose of illustrating the vibration isolation performance.

The design optimization of angle $\phi$ should be subjected to the requirement on a specific practical problem. For example, in the case of high-technology precision manufacturing, one should consider to attenuate the vibration in a few concerned directions or all directions simultaneously. In such cases, a reasonable objective function should be established to take into account vibration isolation effectiveness in these directions, and to minimize the overall power flow into the base. Thus optimization is very much objective oriented based on particular requirements, which would be a topic of the authors' future work and not presented in this paper.

Another important parameter is damping, which might have significant effect on the vibration isolation performance of the platform. It depends on the friction between each contacting pair, and might be very difficult to be predicted. However, in the proposed negative-stiffness mechanism, the roller rolls rather than slides on the semi-circular cam. Generally, rolling friction is expected to be much smaller than sliding friction. Moreover, in the authors' previous experimental study [10], a similar cam-roller-spring negative-stiffness mechanism was tested. We investigated the experimental responses of the QZS isolator at different excitation frequencies and amplitudes, and found that the damping ratio remains similar level. Thus in numerical simulations we usually take the damping ratio as a constant value. Surely, for a real application, the damping ratios in different motions should be measured through experiments. In this numerical simulation, the damping ratio is taken at 0.05 in the purpose of illustrating the characteristic of the QZS platform. Of course, there is no difficulty to include different damping ratios in numerical simulations, and the effects of damping on force transmissibility will be discussed in Section 4.4.

It should be noted that the damping ratios selected as 0.05 for simulation is based on the experience on the experimental study [10], and the numerical analysis (using damping ratio 0.05) only indicates the characteristics of the new 6-DOF QZS platform. The actual damping ratios should be obtained by only experiments on a prototype, including the issue on whether the damping ratios are dependent on displacement or not, which is not in the scope of this paper. The purpose of this paper is to propose a design method for 6-DOF QZS platform and illustrate the feature of the new platform.

### 4.1 Cross coupling stiffness

The force-displacement relationships in all individual directions have been presented previously in Eqs. (30) to (35), which indicate that this platform has QZS characteristics in each individual DOF. However, the restoring force is not only related to the displacement in the direction of the force, but also fully coupled with displacements in other directions. Figs. 7 and 8 illustrate force-displacement relationships of $\bar{F}_z$ and $\bar{M}_z$, respectively, in cross coupling planes. Note that the force-displacement relationships in a cross coupling plane are obtained from Eqs. (24) -(29) by letting other displacement variables out of the cross coupling plane be zero. For example, the expression of $\bar{F}_z$ in *zx* plane can be explicitly given by

$$\bar{F}_z = \frac{\gamma}{4\cos^2\phi}\left(4c^4\bar{z}^3 + 6c^2s^2\bar{x}^2\bar{z} - 4cs^3\bar{x}^3\right) \tag{50}$$

For the fake of brevity, other four forces are not shown, which are similar to $\bar{F}_z$ and $\bar{M}_z$.

It can be seen that the non-zero displacement in non-loading direction can introduce a linear term, and even a quadratic term, into the force-displacement relationship, which can result in an interference to the loading direction from other DOFs, and cause an increase in the stiffness of the system. Hence, the cross coupling effect is undesirable in terms of vibration isolation. Fortunately, from Figs. 7 and 8, it can be observed that

there exist large flat areas on the curved surfaces of force-displacement relationships. It means that the stiffness is small in a large displacement space near the static equilibrium position (0, 0, 0, 0, 0, 0). Moreover, the stiffness at the static equilibrium position always remains zero. Therefore, the cross coupling has an insignificant influence on the 6-DOF QZS characteristics of this platform, when oscillations are close to the static equilibrium.

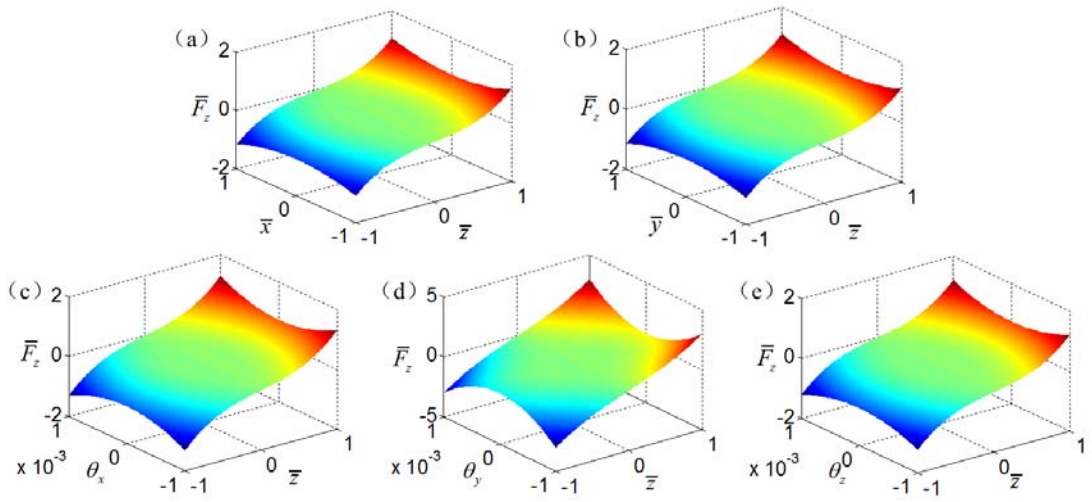


Fig 7 Force-displacement relationship of $\bar{F}_z$ in (a) $zx$ plane, (b) $zy$ plane, (c) $z\theta_x$ plane, (d) $z\theta_y$ plane, and (e) $z\theta_z$ plane.

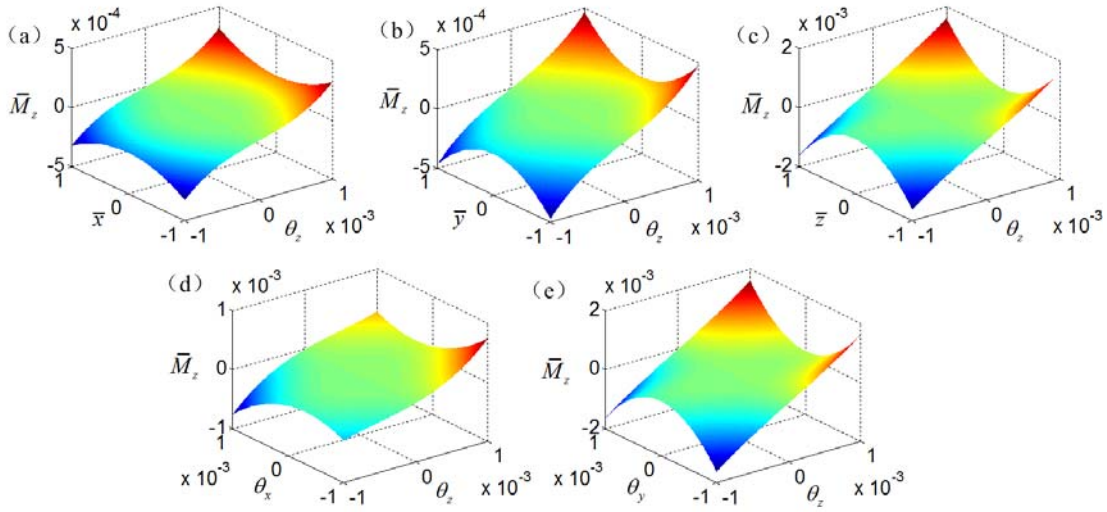


Fig 8 Force-displacement relationship of $\bar{M}_z$ in (a) $\theta_z x$ plane, (b) $\theta_z y$ plane, (c) $\theta_z z$ plane, (d) $\theta_z \theta_x$ plane, and (e) $\theta_z \theta_y$ plane.

### 4.2 Characteristics of amplitude-frequency relationship

The amplitude-frequency relationships can be obtained by solving the nonlinear algebraic Eqs. (47), as shown in Fig. 9. The solid lines and dotted lines denote stable and unstable solutions, respectively, and the hollow circles represent the numerical solutions by using both the forward and backward frequency sweeps. For the frequency sweeps, the time histories of displacements are obtained by solving the equations of motion (Eqs. (41)) using the Runge–Kutta algorithm, and then the maximum amplitudes of steady-state displacement responses are collected as the numerical results.

It can be seen from Fig. 9a and Fig. 9b that, in the two frequency ranges of 0.005 to 0.266 and 0.65 to 1, there exist gaps between numerical solutions and theoretical approximations, which can be attributed to the fact that, in those frequency ranges, the system experiences complicated dynamical behaviour, such as sub/super-harmonic motion, quasi-periodic motion and even chaotic motion. Since the Harmonic Balance method only includes the effect of the fundamental harmonic component, thus the first approximation cannot match well with the responses containing multi-harmonic components in such two frequency ranges, as shown in Figs. 9a and 9b. In contrast, out of these two frequency ranges, there is exceptional agreement between theoretical and numerical results, especially for small-amplitude oscillations.

As seen from the expressions of the stiffness of the linear platform, i.e. Eq. (39), the stiffness in each DOF is decoupled, in other words, the force is independent of displacements in other DOFs. Thus, only one peak occurs on the amplitude-frequency curve for the linear system. However, there exist two or more peaks for the QZS system, due to the stiffness coupling effects, which normally appear in low-frequency range when the platform undergoes large-amplitude vibrations, as shown in Figs. 9a and 9b.

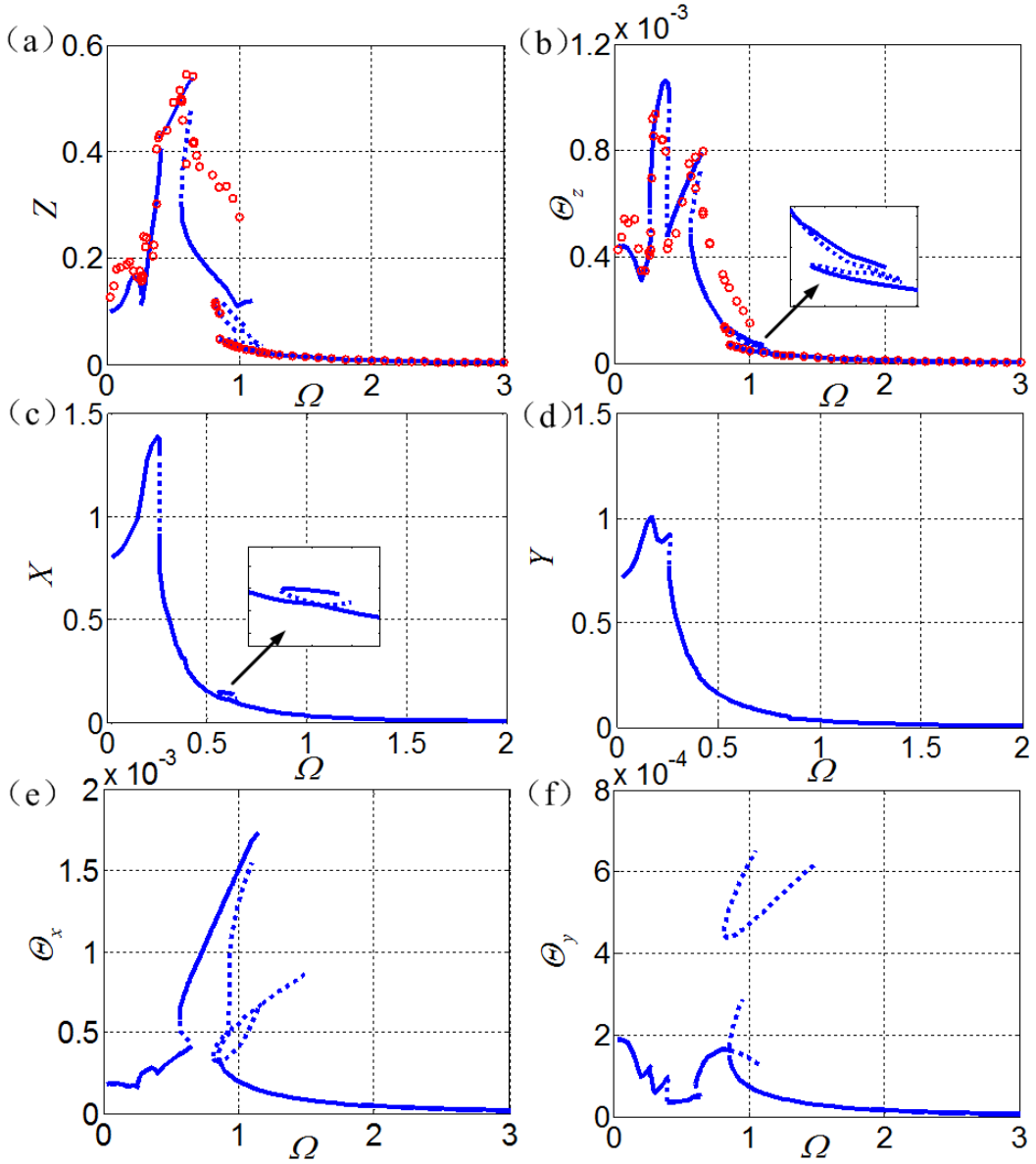


Fig 9 Fundamental responses (amplitude *vs* frequency curves) of the system, (a) $Z$, (b) $\Theta_z$ (c) $X$, (d) $Y$, (e) $\Theta_x$, (f) $\Theta_y$. Solid lines and doted lines denote stable and unstable solutions, respectively, and cycle dots represent numerical solutions of both the forward and backward frequency sweeps.

### 4.3 Force transmissibility

The vibration isolation performance is evaluated by the force/moment transmissibility in each DOF, as defined by Eq. (49), which is depicted in Fig.10. It should be noted that the transmissibility curves seem discontinuous, since unstable solutions are not depicted. Theoretical results are verified by numerical simulations, as illustrated by dots in Figs. 10a and 10b. Due to the complicated form of responses, the numerical

results of transmissibility are given in a statistical form, which is defined as the ratio of root mean square (RMS) of transmitted forces to those of excitations [10] in decibel, i.e.

$$T_{\mathrm{NS}} = 20\log_{10}\left(\frac{\mathrm{RMS}\left[\bar{F}_{\mathrm{T}}\left(\bar{t}_i\right)\right]}{\mathrm{RMS}\left[\bar{F}\left(\bar{t}_i\right)\right]}\right) \tag{51}$$

where $\bar{F}_{\mathrm{T}}\left(\bar{t}_i\right)$ and $\bar{F}\left(\bar{t}_i\right)$ are time histories of the transmitted force and the excitation in each DOF, respectively. Based on the time histories of displacements $\bar{\mathbf{u}}$ and velocities $\bar{\mathbf{u}}'$, obtained by numerically solving the equations of motion, the force transmitted to the base can be given by

$$\bar{\mathbf{F}}_{\mathrm{TN}} = 2\boldsymbol{\zeta}\bar{\mathbf{u}}' + \bar{\mathbf{F}}_{\mathrm{R}}\left(\bar{\mathbf{u}}\right) \tag{52}$$

As seen from Figs. 10a and 10b, there exist differences between theoretical and numerical results in several low frequency ranges, because of the complicated responses rather than periodic motions with sole harmonic component. However, theoretical results agree with numerical simulations well in most of the frequency range, especially in the effective frequency range of vibration isolation. Moreover, the predication of jump phenomenon is also closely validated by numerical simulations. Therefore, the theoretical transmissibility is capable of evaluating vibration isolation performance of the 6-DOF QZS platform system.

As a counterpart, the theoretical transmissibility of the linear platform is also illustrated in Fig. 10, as denoted by dashed lines, which has a single peak due to the decoupling stiffness, as mentioned previously. From Fig.10, the advantage of the QZS system can be observed evidently in all DOFs, although the advantages in *x* and *y* translational DOFs are less obvious than those in other DOFs. Specifically, the advantages can be mainly summarised up in two points. Firstly, the effective frequency range of vibration isolation is extended into lower frequencies as a result of using the QZS struts, or in other words, the QZS platform has a broader bandwidth of vibration isolation than its liner counterpart. Secondly, in the effective frequency

range, the force transmissibility is much lower than that of its linear counterpart, especially in low frequency range, which means that the QZS platform possesses much higher performance of vibration isolation than its linear counterpart. Most importantly, such good performances occur in all six DOFs.

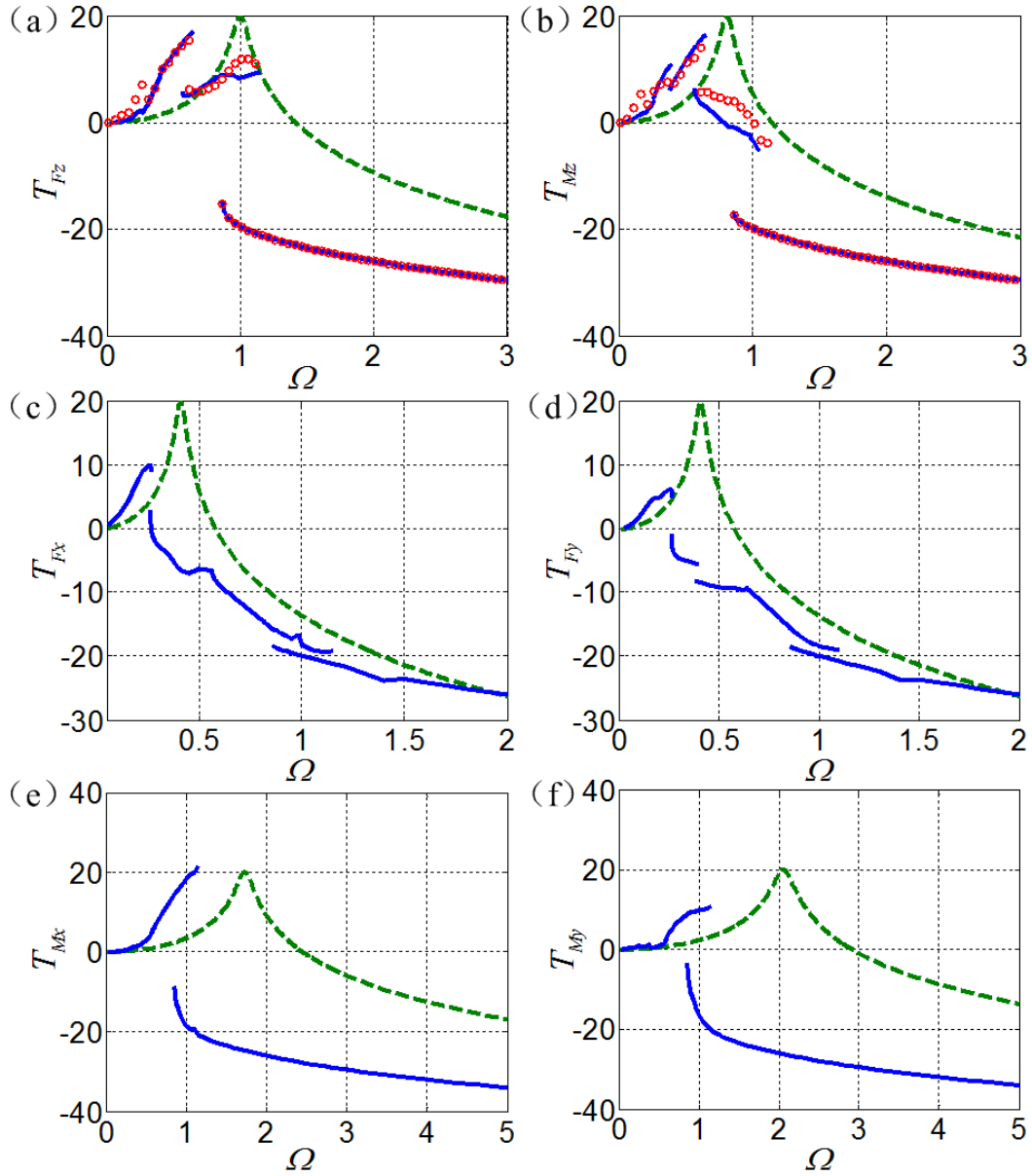


Fig 10 Transmissibility in each DOF, (a) $T_{Fz}$, (b) $T_{Mz}$, (c) $T_{Fx}$, (d) $T_{Fy}$, (e) $T_{Mx}$, (f) $T_{My}$. Solid lines and dots denote stable theoretical and numerical results, respectively, of the QZS system; dashed lines represent results of the counterpart linear system.

For the force transmissibility in *x* and *y* translational DOFs, jumps occur in the

effective frequency range of vibration isolation, because of the stiffness coupling effects, as shown in Figs. 10c and 10d. However, the transmissibility on the upper branch is still below that of the linear counterpart. Therefore, although the cross coupling effects might affect vibration isolation performance in certain DOFs, it hardly loses its advantage over its linear counterpart.

### 4.4 Effects of damping on force transmissibility

The effects of damping on force transmissibility are depicted in Fig. 11. For the sake of brevity, only the transmissibility in the DOFs of $z$ and $\theta_z$ are considered here. Note that the effects of damping in other DOFs are similar to those in such two DOFs. From Figs. 10a, 10b, and 11, it can be observed that as the damping increases, the peak transmissivity decreases, and the solution structure, which is dependent on the intensity of stiffness coupling, becomes simple. Moreover, the jump phenomenon is supressed effectively by increasing damping, and thus under a comparatively heavy damping, the jump phenomenon is expected to be completely avoided.

Additionally, the increasing damping lowers the beginning frequency of vibration isolation, and thus broadens the bandwidth of vibration isolation, due to the fact that the resonance and jump phenomenon are supressed effectively by the increasing damping. However, in the effective frequency range, the force transmissibility rises as the damping increases, which means a reduction in vibration isolation effectiveness. Therefore, a moderate damping is capable of supressing resonance, avoiding jump phenomenon and keeping good overall performance in the effective frequency range of vibration isolation simultaneously.

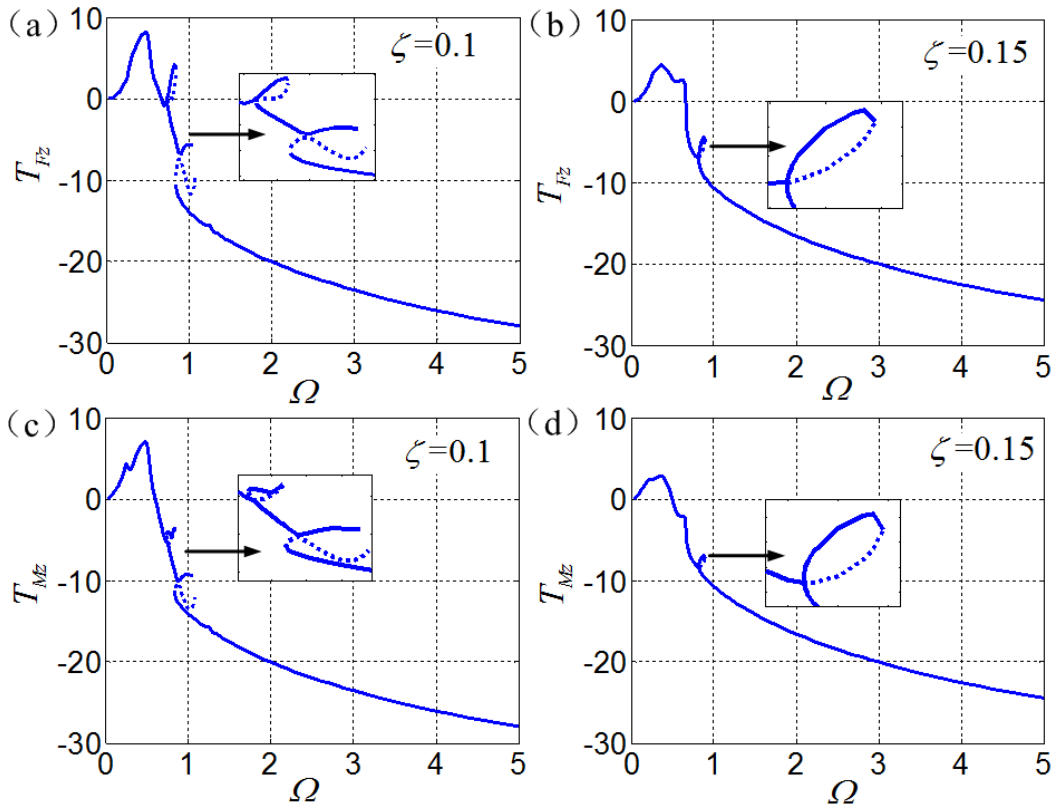


Fig 11 Effects of damping on the force transmissibility. (a) $T_{Fz}$, $\zeta$=0.1; (b) $T_{Fz}$, $\zeta$=0.15; (c) $T_{Mz}$, $\zeta$=0.1; (d) $T_{Mz}$, $\zeta$=0.15. Solid lines: stable solutions; dotted lines: unstable solutions.

## 5 Conclusions

A conceptual design of a quasi-zero-stiffness (QZS) platform supported by novel QZS struts is proposed for low-frequency vibration isolation in six degrees of freedom (DOFs). The static analysis of the platform is carried out, and then, considering excitations in all six DOFs, the equations of motion of the platform are established, which are solved by using the Harmonic Balance method. Finally, the performance of vibration isolation is evaluated in terms of transmissibility, and the stiffness coupling effects on amplitudes and transmissibility are also discussed.

It is found that this vibration isolation platform has QZS characteristics in all six DOFs, and substantially outperforms its linear counterpart. Specifically, by using the proposed QZS struts, the bandwidth of vibration isolation is broadened into lower

frequency, and the effectiveness of vibration isolation is notably improved. Most importantly, such advantages occur in all six DOFs, which is desired in many real engineering applications, such as high precision manufacturing and equipment protection in spacecraft. The cross coupling effects might be active when the platform undergoes large-amplitude oscillations, which usually appear at low frequency but out of the effective frequency range of vibration isolation, and thus such cross coupling hardly degrades the performance of the QZS platform. Additionally, a moderate damping is needed to supress resonance, avoid jump phenomenon, and keep good overall vibration isolation effectiveness simultaneously.

## 6 Acknowledgments

This research work was supported by National Natural Science Foundation of China (11572116, 11402082), Natural Science Foundation of Hunan Province (2016JJ3036), and Fundamental Research Funds for the Central Universities. A large part of this work is carried out during the first author’s visit to the University of Liverpool.

## Reference

[1] P. Alabuzhev, A. Gritchin, L. Kim, G. Migirenko, V. Chon, P. Stepanov, Vibration protecting and measuring system with quasi-zero stiffness, Taylor & Francis Group, New York, 1989.

[2] R.A. Ibrahim, Recent advances in nonlinear passive vibration isolators, Journal of Sound and Vibration 314(3-5) (2008)371-452.

[3] W.G. Molyneux, The Support of an Aircraft for Ground Resonance Tests, Aircraft Engineering and Aerospace Technology 30(6)(1958)160 - 166.

[4] A. Carrella, M.J. Brennan, I. Kovacic, T.P. Waters, On the force transmissibility of a vibration isolator with quasi-zero-stiffness, Journal of Sound and Vibration 322(4-5)( 2009) 707-717.

[5] I. Kovacic, M.J. Brennan, T.P. Waters, A study of a nonlinear vibration isolator with a quasi-zero stiffness characteristic, Journal of Sound and Vibration 315(3)(2008) 700-711.

[6] Z. Hao, Q. Cao, The isolation characteristics of an archetypal dynamical model with stable-quasi-zero-stiffness, Journal of Sound and Vibration 340(2015) 61-79.

[7] D. Xu, Y. Zhang, J. Zhou, J. Lou, On the analytical and experimental assessment of performance of a quasi-zero-stiffness isolator, Journal of Vibration and Control 20(15)( 2014) 2314-2325.

[8] C.-C. Lan, S.-A. Yang, Y.-S. Wu, Design and experiment of a compact quasi-zero-stiffness

isolator capable of a wide range of loads, Journal of Sound and Vibration 333(20)(2014) 4843-4858.

[9] T.D. Le, K.K. Ahn, A vibration isolation system in low frequency excitation region using negative stiffness structure for vehicle seat, Journal of Sound and Vibration 330(2011) 6311-6335.

[10] J. Zhou, X. Wang, D. Xu, S. Bishop. Nonlinear dynamic characteristics of a quasi-zero stiffness vibration isolator with cam-roller-spring mechanisms, Journal of Sound and Vibration 346(2015) 53-69.

[11] J. Zhou, D. Xu, S. Bishop, A torsion quasi-zero stiffness vibration isolator, Journal of Sound and Vibration 338(2015) 121-133.

[12] D. Platus, Negative-stiffness-mechanism vibration isolation systems, Proceedings of the SPIE's International Symposium on Vibration control in Microelectronics, Optics and Metrology, 1991.

[13] X. Liu, X. Huang, H. Hua, On the characteristics of a quasi-zero stiffness isolator using Euler buckled beam as negative stiffness corrector, Journal of Sound and Vibration 332(14)( 2013)3359-3376.

[14] C.M. Lee, V.N. Goverdovskiy, A.I.Temnikov, Design of springs with "negative" stiffness to improve vehicle driver vibration isolation, Journal of Sound and Vibration 302(4)(2007) 865-874.

[15] A.D. Shaw, S.A. Neild, D.J. Wagg, P.M. Weaver, A. Carrella, A nonlinear spring mechanism incorporating a bistable composite plate for vibration isolation, Journal of Sound and Vibration 332(24)(2013) 6265-6275.

[16] Q. Li, Y. Zhu, D. Xu, J. Hu, W. Min, L. Pang, A negative stiffness vibration isolator using magnetic spring combined with rubber membrane, Journal of Mechanical Science and Technology 27(3)(2013) 813-824.

[17] D. Xu, Q. Yu, J. Zhou, S.R. Bishop, Theoretical and experimental analyses of a nonlinear magnetic vibration isolator with quasi-zero-stiffness characteristic. Journal of Sound and Vibration 332(14)(2013) 3377-3389.

[18] Y. Zheng, X. Zhang, Y. Luo, B. Yan, and C. Ma, Design and experiment of a high-static–low-dynamic stiffness isolator using a negative stiffness magnetic spring, Journal of Sound and Vibration, 360(2016) : 31-52.

[19] W. Wu, X. Chen, Y. Shan, Analysis and experiment of a vibration isolator using a novel magnetic spring with negative stiffness. Journal of Sound and Vibration 333(13)(2014) 2958-2970.

[20] A. Carrella, M.J. Brennan, T.P. Waters, K. Shin, On the design of a high-static-low-dynamic stiffness isolator using linear mechanical springs and magnets, Journal of Sound and Vibration 315(3)(2008) 712-720.

[21] W. Robertson, M. Kidner, B. Cazzolato, A. Zander, Theoretical design parameters for a quasi-zero stiffness magnetic spring for vibration isolation, Journal of Sound and Vibration 326(1-2)( 2009) 88-103.

[22] X. Sun, X. Jing, J. Xu, L. Cheng, Vibration isolation via a scissor-like structured platform, Journal of Sound and Vibration 333(9)( 2014) 2404-2420.

[23] Y. Araki, T. Asai, K. Kimura, K. Maezawa, T. Masui. Nonlinear vibration isolator with adjustable restoring force, Journal of Sound and Vibration 332(23)(2013) 6063-6077.

[24] Y. Wang, H.-J. Liu. Six degree-of-freedom microvibration hybrid control system for high technology facilities, International Journal of Structural Stability and Dynamics 9(3)(2009) 437-460.

[25] J. Winterflood, High performance vibration isolation for gravitational wave detection, PhD Thesis, University of Western Australia, Perth, 2001.

[26] W.-Y. Zhou, D.-X. Li. Design and analysis of an intelligent vibration isolation platform for reaction/momentum wheel assemblies. Journal of Sound and Vibration 331(13)(2012) 2984-3005.

[27] D. Kamesh, R. Pandiyan, A Ghosal, Passive vibration isolation of reaction wheel disturbances using a low frequency flexible space platform, Journal of Sound and Vibration 331(6)( 2012)1310-1330.

[28] M. E. Hoque, T. Mizuno, Y. Ishino, M. Takasaki, A six-axis hybrid vibration isolation system using active zero-power control supported by passive weight support mechanism, Journal of Sound and Vibration 329(17)( 2010) 3417-3430.

[29] X. Sun, X. Jing, Multi-direction vibration isolation with quasi-zero stiffness by employing geometrical nonlinearity, Mechanical Systems and Signal Processing, 62–63(2015) 149-163.

[30] T. Zhu, B. Cazzolato, W. Robertson, A. Zander. Vibration isolation using six degree-of-freedom quasi-zero stiffness magnetic levitation, Journal of Sound and Vibration 358(2015) 48-73.

[31] Z. Wu, X. Jing, B. Sun, F. Li, A 6DOF passive vibration isolator using X-shape supporting structures, Journal of Sound and Vibration, 380 (2016) 90-111.

[32] R. C. Hibbeler, Mechanics of Materials, Eighth Edition, Prentice Hall, Boston, 2011.